2D-3D computations of a vertical axis wind turbine flow field: modeling issues and physical interpretations

N. Franchina[a,*], G. Persico[b], M. Savini[a]

[a] *Università degli Studi di Bergamo, Dipartimento di Ingegneria e Scienze Applicate, viale Marconi 5 - 24044 Dalmine (BG), Italy*
[b] *Politecnico di Milano, Dipartimento di Energia, Laboratorio di fluidodinamica delle macchine, via Lambruschini 4 - 20156, Milano, Italy*

Abstract

This paper presents the results of a numerical investigation on the flow field past a Vertical Axis Wind Turbine at different operating conditions. Several numerical issues are considered, including the extension of the domain, the class of boundary conditions assigned, the space and time resolution, and the numerical accuracy in the resolution of the equations. The inlet boundary condition and the physical position where it is assigned, as well as appropriate far field conditions, are shown to be crucial for the reliability of the computed turbine performance. Notice that using proper boundary conditions and numerical settings allows to employ not too large computational grids. The conclusions obtained are strengthened by a detailed comparison with a large data-base of experiments available for the turbine under consideration, that include both performance and time-resolved velocity measurements in the wake. The resulting flow model is then used to run time-accurate two-dimensional (2D) and three-dimensional (3D) simulations of the flow around the turbine. This set of simulations is exploited in combination to dedicated studies on the unsteady profile aerodynamics as well as detailed three-dimensional measurements in the wake to provide consistent physical interpretation of the computed flow fields.

Keywords:
VAWT, RANS modeling, 2D-3D VAWT performance prediction

*Corresponding author, nicoletta.franchina@unibg.it, +390352052084

Nomenclature

c	blade chord $[m]$
f	reduced frequency [–]
k	turbulent kinetic energy $[m^2/s^2]$
n	rotational speed $[rad/s]$
A	swept area A=HD $[m]$
C_D, C_L	drag and lift coefficient $C_{D,L}$=D,L/(1/2 $\rho_\infty V_\infty^2$A) $[-]$
C_M	moment coefficient C_M=M/(1/2ρ_∞ V_∞^2 AR) $[-]$
C_P	power coefficient $C_P = C_M \lambda$ $[-]$
D	turbine diameter $[m]$, drag $[N]$
L	lift $[N]$
H	turbine span $[m]$
M	moment $[Nm]$
N	blade number $[-]$
P	power $[W]$
R	turbine radius $[m]$
RANS	Reynolds Averaged Navier-Stokes
Re	Reynolds number $[-]$
SST	Shear Stress Transport
TSR	Tip Speed Ratio
Tu	turbulence intensity Tu= $\sqrt{2k/3}/V_\infty$ $[-]$
U	peripheral velocity $[m/s]$, uncertainty [-]

V	absolute velocity $[m/s]$
VAWT	vertical-axis wind turbine
W	relative velocity $[m/s]$
α	incidence angle $[deg]$
λ	tip speed ratio $[-]$
ρ	air mass density $[kg/m^3]$
σ	solidity σ=Nc/D $[-]$
ω	vorticity $[1/s]$
θ	azimuthal angle $[deg]$
Δt	time step $[s]$
Δx	spatial discretization parameter $[m]$

Subscripts

T	tangential
∞	freestream
1	$\lambda = 3.3$
2	$\lambda = 2.4$

1. Introduction

Wind energy is nowadays one of the most relevant renewable energy sources and, as such, it has been object of several experimental and numerical studies in recent years, oriented both to investigate the wind turbine aerodynamics and to develop more reliable and effective design techniques, with the ultimate goal of enhancing the performance of single rotors and wind farms.

Several technical configurations were proposed to exploit the wind energy, and among them, the horizontal axis wind turbine (HAWT) dominates the market in the range of medium-to-large power installations. For small power capacity, the vertical axis wind turbine (VAWT) may represent an interesting alternative, as it does not require a yaw orientation system, it is characterized by lower costs of installation and maintenance, and it produces lower acoustic pollution, thus resulting better suited for urban installation. On the opposite side of very large-scale, VAWTs are also considered for deep-sea off-shore application with floating foundations, mainly due to structural reasons [1].

Despite the aforementioned constructive and operation advantages, the VAWT rotors are characterized by a very complex aerodynamics, which are inherently unsteady, fully three-dimensional, typically transitional in small-scale applications ($Re_c < 10^5$), and prone to flow-separation on the blades (see *e.g.* [2] for a description). During a blade revolution the angle of attack and the relative velocity perceived by the profile change continuously, resulting in an instantaneous fluctuation of forces and torque acting on the turbine. A comprehensive review of the basic aerodynamics as well as the simplified design and analysis models available for VAWTs is reported by Parachivoiu [3].

In recent years, the significant increase of available computational power has opened the way to approach the calculation of VAWTs by means of advanced Computational Fluid Dynamics (CFD), that is rapidly becoming a common analysis tool for this class of machines. However, such simulations require a very large computational cost which makes these models still prohibitive for design purposes and has historically led the researchers to employ simplified actuator-line or 2D flow models, which involve a much reduced computational requirement.

Simplified 2D models were used to investigate dynamic stall at low Reynolds number for a single oscillating blade in comparison to experiments [4], showing the effectiveness of SST $k - \omega$ models for a reasonable prediction of complex vortical structures developing during pitching motion. 2D computations on a three bladed VAWT were also performed to investigate complex transitional effects [5], highlighting how the stall onset is predicted earlier when transitional models are adopted with the $k-\omega$ model. From the technical perspective, 2D models allow to capture relevant physical effects such as dynamic stall and turbulence modeling, but fail in producing reliable estimates of power coefficients, due to struts, trailing vortices, tip losses, spanwise flow divergence due to blockage effect, *etc.*. These issues have been studies in [6], which focuses on different turbulence modeling and on the feasibility of 2D and 2.5D simulations, by virtue of both URANS and LES. The authors indicate that overprediction of C_P of 2D URANS is mainly due to the inability in reproducing the airfoils aerodynamic performance at high angle of attack, and they also show that 2.5D LES can give good agreement with experiments at relatively low TSR. A recent study [7] has shown that proper correction terms for strut and tip losses can upgrade significantly the reliability of 2D models in predicting H-shape VAWT performance.

However, with the aim of constructing a high-fidelity simulation tool for VAWTs, the formulation of a 3D CFD model which requires a technically-acceptable computational cost still remains a relevant challenge. Moreover, if complex VAWT architectures are considered (such as troposkien or swirling layouts), only a fully 3D model can provide reliable performance estimates.

To the authors' best knowledge, only a few 3D studies have been published on VAWT simulations. 3D URANS results of VAWT in skewed flows are presented in [8], 2D and 3D models are applied in [9] for aerodynamic modeling and in [10] to investigate self-starting capability of VAWT. It is to be noted that 3D computational grids employed must often appear as rather coarse with respect to the 2D counterparts, to meet the constraints in computational cost($y^+ \simeq 5$, $2-10$ millions cells, see for example [11]). The most advanced attempt of a fully 3D simulation of a VAWT is reported in [12] in which a single-blade configuration was considered due to restrictions in computational cost.

The challenge of constructing a feasible but reliable 3D flow model of VAWTs requires to consider several numerical parameters that are of great importance to achieve feasible results. The space discretization, the extension of the discrete domain, the boundary conditions, the turbulence modeling are among the most important issues. Time step size is another crucial parameter in unsteady flow and is of particular relevance for VAWT analysis, due to their inherent unsteady aerodynamics. Several investigations have already been presented in literature for the assessment of mesh and step size requirements in CFD for the simulation of VAWT. The two parameters are strongly connected, and furthermore are not independent of the device operating conditions.

In [13] a thorough investigation on numerical settings, time step size, domain definition is presented. In particular, they have found that the angular time-step ranges between $1/15^\circ$ and 2°. [14] investigated, through 2D computations, two operating VAWT conditions for which they suggested to employ a time step equal to $1/30^\circ$. From these studies, consistent and coherent guidelines can be deduced on the space/time discretization.

Turbulence models have also a significant impact on the quality of the numerical solution, due to the large angle of attack and the subsequent potential onset of stall on the profile. Even though these features would justify LES or DNS approaches, their prohibitive computational cost and the immediate industrial interest of VAWT has led most researchers to focus on the capabilities of RANS model, that is the framework in which also the present computational study is performed. A review of the open Literature (see *e.g.*, [4], [9], [14], [13], [15]), provides a very clear indication on the necessity of using two-equation turbulence models with proper near-wall treatment for time-varying aerodynamic problems in presence of large incidence fluctuations. In particular, the simulations reported in [7] showed indeed that the SST $k - \omega$ model performs well in VAWT flow computations against experiments.

Less established guidelines are, instead, available, for other key issues of these simulations, such as the dimension of the computational domain and the set of boundary conditions. 2D simulations often employ very large domains, up to 40 and 100 turbine diameters upstream and downstream of the turbine respectively, and a width up to 60 diameters (*e.g.* [14, 16, 13]). Such domains, however, may lead to prohibitively large extensions in three dimensions. In fact, the few available 3D studies employ smaller domain (*e.g.* 5-10 diameters upstream and on the sides, 10-15 diameters downstream, see [17, 9, 11]); it is evident that, in these cases, detailed experimental comparisons are required for assessment and the set of conditions assigned on the external boundary of the domain need a reconsideration.

In light of the present State of the Art of VAWT simulation models, the present paper discusses the reliability of standard second-order accurate 2D and 3D computations, performed using two commercial codes, by means of systematic comparison with the experimental data coming from a wide test campaign performed in a large-scale wind tunnel. Relevant computational parameters are considered to investigate the sensitivity of the flow model to the computational settings and to investigate if high quality results can be obtained at a reasonable (namely, industrially relevant) computational cost. To this end a key issue of the present study is the extent of the simulation domain, which must be large enough to avoid artificial blockage effects but as small as possible to allow reducing the computational cost. In particular we investigate the boundary placement with respect to the blockage effect and its influence on the performance prediction through comparison with experimental measurements of the rotor wake. Proper boundary conditions must be adopted according to the physical aspects. Unsteady RANS computations are then here presented to both investigate the reliability of 2D and 3D computations and to study complex flow features characterizing the flow around a vertical axis wind turbine.

2. Case study

The turbine considered for the present study is a real-scale model of a VAWT for micro-generation (P_{max}=200W). The rotor features a straight H-shape, it is composed by three unstaggered NACA0021 blades, with a chord of 0.0086 m and length equal to 1.46 m; the turbine diameter is 1.03 m (resulting in a swept area of about 1.5 m^2). Figure 1 displays the turbine configuration including the supporting structure given by two flat radial elements. The main geometrical characteristics of the turbine considered are reported in Table 1. Full details on

Blade height	1.457 m
Rotor diameter	1.030 m
Solidity	0.25
Chord	0.086 m
Blade airfoil	NACA0021

Table 1: VAWT geometric parameters

the turbine geometrical features as well as on the turbine operating and performance parameters can be found in [18]. In the present study, two operating configurations are considered, one close to the peak C_p condition and one at high-load operation, whose details are reported in Table 2.

2.1. Experiments

The VAWT model was object of a wide experimental campaign carried out in the large-scale wind tunnel of the Politecnico di Milano (Italy). The wind tunnel features a 6-meter long test section of square cross area of about 16 m^2, where relatively high speed flows (up to 50 m/s) are generated with very low turbulence (below 1%). In order to minimize the blockage induced by the wind tunnel walls, the tests considered for the present study were performed in unconfined configuration, removing the test room so that a free-jet is released to the rotor, which is placed in the center of the jet. The application of dedicated correlations for free-jet blockage [19] indicates that the blockage effect, for the

V[m/s]	TSR	C_P	$U_{C_P[95\%]}$
6.54	3.3	0.154	0.017
9.00	2.4	0.277	0.034

Table 2: Working conditions

present case, is below 1.5%, and hence it was neglected for the subsequent discussion.

As documented in full detail in [18], several measurement techniques were applied within the test campaign. Performance predictions were achieved by combining angular speed with torque measurements, respectively obtained with an absolute encoder and a precision torque meter. Different levels of uncertainty resulted for different TSR, and are given in Table 2 for the conditions of interest of this work.

Velocity and turbulence measurements were performed in the wake by traversing multiple hot wires downstream of the rotor. The set of hot wire probes provided time-resolved measurements of both streamwise and cross-stream velocity components with uncertainty of about 2%. A proper data-processing technique, reported extensively in [20], was performed to extract from the time-resolved hot-wire signals the time-averaged, phase-resolved, and turbulent components of the velocity; this latter was used to determine the streamwise turbulence intensity.

A pneumatic five-hole probe was also traversed in the turbine wake to measure the pressure level and the 3D flow direction, with related uncertainties within 10 Pa in pressure and ± 0.2 deg in the flow angles. Measured pressure values confirmed the absence of blockage-induced overspeed outside the wake region; as shown in [21], flow angle measurements indicate the fully 3D character of the velocity field in the wake of this turbine, especially in the tip region where large-scale trailing vortices are released downstream. This motivates the relevance of fully 3D computations for this class of machines.

2.2. Computational models

The flow field characterizing a VAWT is unsteady and incompressible (the relative Mach number is always lower than 0.1), and the regime is turbulent. In this work we consider a modeling based on RANS equations, *i.e.* the equation of mass and momentum conservation along with the two-equation model $k-\omega$ SST developed by Menter [22] which is the most used two equation turbulence

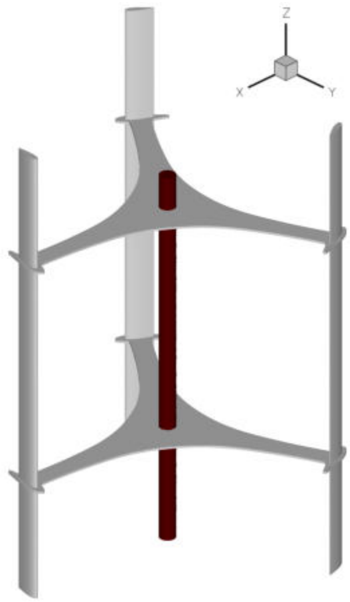

Figure 1: Wind turbine geometry

model in turbomachinery applications. In fact, the SST $k-\omega$ model as reported in the open Literature (see, for example, [4, 16, 14, 15]) provides a very clear indication on the necessity of using two-equation turbulence models with proper near-wall treatment for time-varying fluid dynamic problems in presence of large incidence fluctuations. Moreover, the 2D simulations of Bianchini and collaborators [7] showed indeed that the SST $k-\omega$ model performs well in VAWT flow computations against experiments. This is because large separation regions and severe adverse pressure gradients take place on the blades depending on the working configuration and during the blade revolution.

In this work, computations have been performed using the commercial codes Fluent®-Ansys v.17 [23] and STAR-CCM+® [24] with the same discretization and modeling settings. The investigation is not intended as a comparison between codes, instead the codes have been used as predictive tools to assess the feasability of our observations. The discretization employed is second-order accurate both in space and time (on a regular enough mesh) and the solution of the unsteady RANS equations has been carried out using a constant time step equal to half a degree of revolution. The solution of the discrete problem has been performed using the pressure-based coupled algorithm in which the system of the momentum equations and the pressure correction equation is solved in a coupled manner, while the turbulence model equations are still solved in a decoupled way. Notice that the coupled algorithm is characterized by an improved convergence rate but involves an increase memory requirement.

The nonlinear system arising at each time step is solved using AMG solver up to an accuracy level of 10^{-5} measured by the norm of scaled residuals. Convergence of the computations is instead evaluated by monitoring the time variation of relevant physical values, such as the power coefficient.

The computational domain is composed of two parts, an inner one, which defines the discretization of the moving part (the turbine with the shaft and the airfoil sections), and an outer one, which defines the steady far field region. The sliding mesh technique is used to deal with the rotation of the turbine; thus an interface boundary condition is used to transfer the informations between the fixed and rotating regions.

The wind turbine rotating regime is 400 rpm and two operating conditions are studied, namely $\lambda = 3.3$ and 2.4, corresponding respectively to the wind freestream velocity of $V_{\infty,1}$=6.54 m/s and $V_{\infty,2}$=9 m/s. The Reynolds number based on the peripheral velocity and the airfoil chord is $1.2 \cdot 10^5$. At the inlet boundary are imposed the velocity, a 1% turbulence intensity (the experimental value) and a viscosity ratio ν_t/ν equal to one, which is a typical value adopted with this turbulence model. At the outlet boundary, pressure is prescribed, and in case of backflow, fluid is entrained at ambient total pressure and temperature. At solid wall the dissipation rate is imposed using the wall boundary condition of Wilcox [25]. Remind that the $k - \omega$ models were designed to be applied throughout the boundary layer, provided that the near-wall mesh resolution is sufficient $y^+ \approx 1$. Both in Fluent and STAR-CCM+, for fine enough meshes, the appropriate low-Reynolds number boundary conditions are applied, with ω

at the wall computed as

$$\omega_w = \frac{\rho(u^*)^2}{\mu}\omega^+$$

where the asymptotic value in the laminar sublayer is computed as described by Wilcox, prescribing the specific dissipation as a function of wall roughness. STAR-CCM+ imposes this condition in the cases of low Reynolds number and of the so called " all y+" wall treatment.

3. Two-dimensional computations

3.1. Numerical issues

In recent times there has been a lot of interest in the literature about various aspects of VAWT simulations, as e.g. the accuracy of 2D computations, the use of low Reynolds number turbulence models, the extent and finesses of the numerical grid, both in time and space, the inlet and outlet (far) boundary conditions to impose. The debate is still open and different authors often came to different conclusions; moreover the correct answers may, and indeed do, change according to the TSR under investigation. As a typical example let us consider the first item, i.e. the expected variation between a 2D simulation and the actual turbine behaviour, in the simplifying case of uniform velocity at inlet and flow symmetry about the midspan plane, as in our wind tunnel experiments where the flow was steady and there was no wind boundary layer. With simple physical reasoning, it is evident that the discrepancy in C_M will increase with the TSR as the losses related to strut friction and to the tip blade effects (in this case the main causes of difference with a 3D flow) roughly increase with the square of the peripheral speed whilst the torque is made non-dimensional with the square of the approaching velocity. Claiming satisfaction when at tip speed ratios around four (standard for a VAWT) the computed two-dimensional C_P is very close to the experimental value is nonsense. Concerning the turbulence model which is most advisable to employ with the computation of separated flows around stalling airfoils and/or with the effect of strong wake impingement on blades (both frequently occurring in a VAWT), experience and open literature suggest to use the SST $k-\omega$ model, coupled with the $low - Re$ option, available in both the commercial codes used in this work. By the way, it is the same recommendation emerging from [4]. We are aware that, using a different and/or more sophisticated (transitional) turbulence model, outcomes can change but a deep investigation of this item alone perhaps deserve a book and is not the aim of our work.

Unless otherwise stated, every 2D simulation carried out in the course of our deep investigation about the above mentioned numerical issues was obtained by means of the Fluent code. When performing 3D computation we however turned to STAR-CCM+, owing to the availability of the 3D software and our better acquaintance with the use of polygonal grids, suited to save computational resources. Of course, all 2D tests selected for the comparison 2D-3D (and quite some other) were done again with the STAR-CCM+ code.

Most tests performed and illustrated in this section were carried out for TSR=3.3 in order to minimize uncertainties arising from the airfoil performance under large variation in the angle of attack, as those experienced at TSR=2.4. In the ideal case of no induced velocity, each profile experiences a periodic variation of the angle of attack α, given by

$$\alpha(t) = \tan^{-1}\frac{\sin[\theta(t)]}{\cos[\theta(t)]+\lambda}, \tag{1}$$

see Figure 2.

The reduced frequency of this phenomenon,

$$f = \frac{nc}{60W} \simeq \frac{c}{2\pi R}, \tag{2}$$

with chord and relative velocity (no induction) selected as reference length and velocity, respectively, is roughly 0.027 and almost independent from TSR. However it can not be inferred that the flow field undergoes quasi-steady changes as, even for λ_1, α varies between $\pm 17.6°$, well beyond the (steady) stall angle of attack, which is about 10 degrees. In this case the crucial frequency becomes the (higher) one associated with stall fluid dynamic perturbations. Moreover,

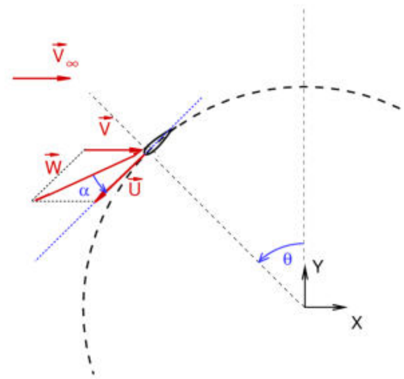

Figure 2: Azimuthal angle θ and flow angle of attack α

in the leeward half revolution, when the flow separates and large vortices are detached from the preceding airfoils, the unsteadiness is strengthened by the incoming wakes and both amplitude and frequency of the disturbances greatly increase.

Since the turbulence model employed computes the flow behavior till the wall, the near-wall space discretization must fulfill the well known requirements on the y^+ value (≈ 1), as well as suitable growing factors within the boundary layer. The "Base" grid chosen is shown in Fig. 3 with a blow-up near the airfoil surface. It consists of 253.800 triangular and quadrilateral cells (213.800 in the inner rotating part and 40.000 in the outer fixed one) with a minimum distance from solid walls of $2 \cdot 10^{-2}$ mm (corresponding to about $2 \cdot 10^{-4}$ chord) and a nearby layer of twelve cells with local widening ratio of 1.2. It extends in all directions three diameters from the VAWT centre of rotation. The good quality of the meshes employed in this work has been checked through the available indicators within the codes such as point distribution, smoothness, and skewness, in particular, maximum aspect ratio is 16 and minimum orthogonality 0.24.

To test the influence of global mesh coarseness, tests were run with finer meshes made of up to 500.000 elements, with the same domain extension of the "Base" grid and similar clustering of points in the boundary layers; the results

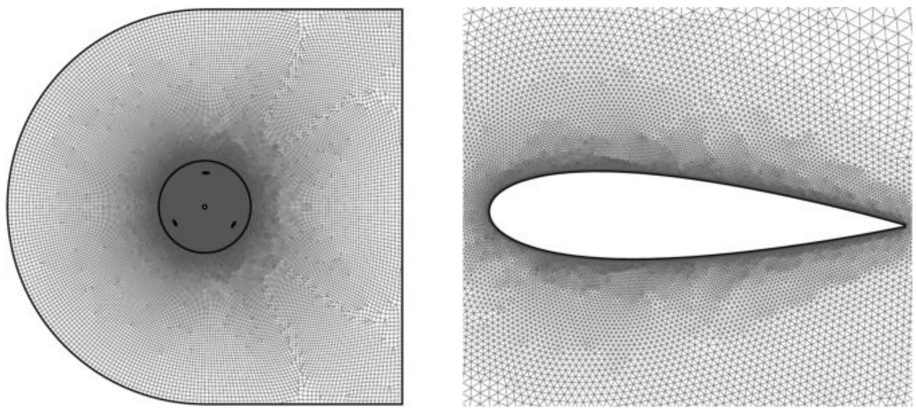

Figure 3: “Base” grid: full domain and airfoil detail

obtained showed no meaningful differences.

Moreover another grid, named “Bl”, was assembled to ascertain the importance of near wall resolution; in this case the minimum distance at walls is reduced to 10^{-5} mm while keeping the same widening law and general characteristic dimensions. Thereby any potential diversity employing the “Base” and “Bl” meshes is only due to first (and following) cell distance from the solid surfaces, and consequent y^+ value. It must be considered that in order to perform a meaningful comparison with 3D computations the number of mesh elements must be kept at a reasonable level, otherwise the request of computational resources blows out of proportion or the comparison lose relevance as the 3D grid finesses is substantially reduced comparing to the 2D one.

Another topic of debate, linked to the previous one, is how far the mesh should extend in all directions to correctly impose the appropriate boundary conditions. The inlet boundary condition (BC) is of course magnitude and direction of the incoming velocity, but different choices are currently adopted regarding downstream and lateral boundaries. We believe that when performing computation simulating an open environment the correct procedure is to impose the value of the static pressure, since the flow field is not at all symmetric nor laterally periodic. We examined the influence of the boundary location building two more grids of the same shape, extending respectively six and nine turbine diameters; let us call them “Med” and “Far” (the latter is shown in Fig 4). It is important to say that each outer grid starts from exactly the inner one; therefore only a strip of cells is added around it without any modification of the previous smaller mesh.

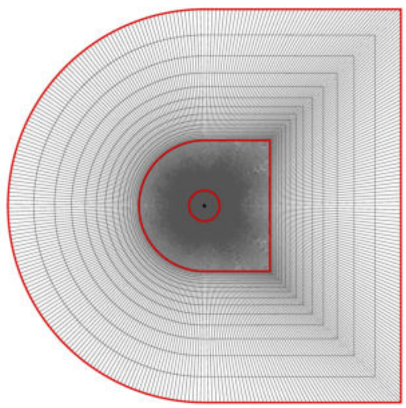

Figure 4: “Far” grid: full domain (inner red line indicates the boundary of the “Base” grid)

One point often underrated when discussing time step size impact on accuracy is that within each time step one has to solve a non-linear algebraic system and the result obtained depends also on the accuracy of this solution. Solver parameters such as “maximum number of iterations per time step” are therefore important and must be varied inversely to the time step size in order to keep the solution of the algebraic system at the same desired level of accuracy specified as “(scaled) residual convergence”. We fixed this parameter at 10^{-5}. Obeying this provision, refinement of the time step beyond 720 steps per revolution (we pushed our investigation down to 7200), i.e. 0.5°, led to negligible difference in the results, as also found by Rezaheya et al. [11].

Table 3 summarizes the average and root mean square value of the computed power coefficient in the last ten revolutions of the turbine, for the four grids considered. As one can notice, a statistically steady periodic solution is finally established in each test case ($C_{P,rms} \leq 10^{-2}\overline{C_P}$) and the “Bl” solution does not substantially differ from the “Base” one. On the contrary, the extent of the computational domain shows its influence, lowering $\overline{C_P}$ when moving to greater

Grid	h_1	$\#D$	$\overline{C_P}$	$C_{P,rms} \cdot 10^2$
"Base"	2	3	0.385	0.213
"Bl"	1	3	0.375	0.289
"Med"	2	6	0.334	0.261
"Far"	2	9	0.291	0.086

Table 3: VAWT λ_1: power coefficient (average and root mean square) for different cases ($h_1/(10^{-4}c)$ first cell off solid wall height, $\#D$ number of rotor diameters off rotor center)

meshes. A local analysis of the static pressure profile along the X coordinate three diameters away from the center in the Y direction, both for "Med" and "Far" grids, pointed out only very small differences with respect to the ambient pressure, there imposed when using the "Base" grid; therefore it can be argued that the responsible for the variation in $\overline{C_P}$ is the inlet boundary condition. Figure 5 shows the non-dimensional velocity magnitude in the half upstream circumference of radius equal to 3D, whilst Figure 6 displays the same variable in a midspan lateral traverse at $X/D = -0.75$, for the three different meshes.

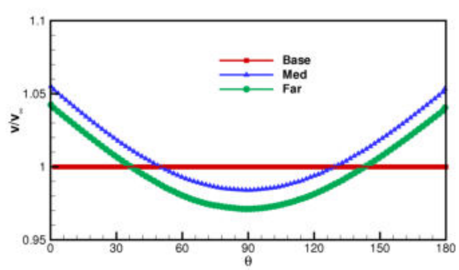

Figure 5: Velocity magnitude distribution along the "Base" grid inlet

It is evident that the position where inlet BCs are assigned influences the flow field and how moving the inlet freestream condition farther upstream there is more room for the deceleration due to the turbine induction effect. In other terms the computations seem to overestimate this effect, even for the "Base" grid, whose inlet (at $Y = 0$) is about at the same upstream distance of wind

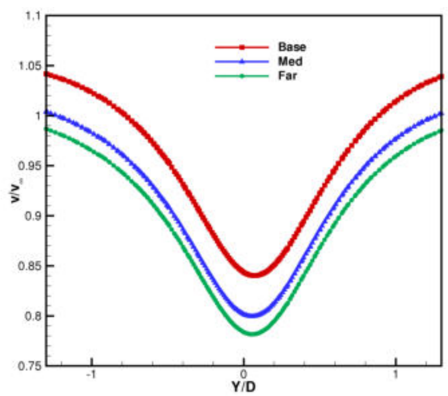

Figure 6: Velocity magnitude distribution at X/D=-0.75

tunnel freestream measurements. In order to limit as much as possible the grid extension, a complete and detailed traverse of (possibly non uniform) measured data should be available at a certain distance; in that case the problem is then trivially solved imposing exactly the experimental data. Proper selection of domain boundaries clearly results in a saving of memory requirements and CPU time.

It must be reminded that, at this wind speed, a 10^{-5} relative error in pressure translates into a 20% error in velocity; therefore any numerical inaccuracy arising from either precision (round-off) errors or approximate knowledge of actual boundary conditions has a dramatic importance.

Turning now the attention to the downstream wake, see Figure 7, one notice that all three numerical traverses lie very close each other and fairly well reproduce the measured profile. In the simulations the time average is performed over one revolution, in the experiments over about thirteen revolutions. The same behaviour takes place at X/D = 1.50. However it is still recognizable a certain level of overspeed, both in the wake and in the outer flow field, not vanishing even for an inlet placed nine diameters far from the centre of rotation. We believe this fact might be due to the peculiar circular shape adopted that forces laterally the flow (in the far field up to $X = 0$). What seems to emerge is that is not at all mandatory to extend downstream and sideways the computational mesh in an excessive manner, but simply to let the flow freely exiting the domain sideways whenever necessary. This can of course be done only provided that neither “slip wall” nor “symmetry” or “periodic” boundary conditions are used. The (upstream) “velocity inlet” should instead be fixed where the actual data are known or reasonably estimated.

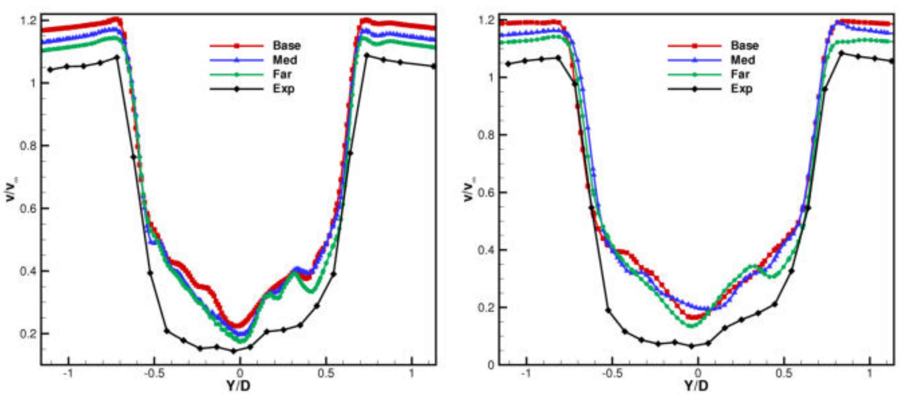

(a) $X/D = 0.75$ (b) $X/D = 1.5$

Figure 7: VAWT λ_1: velocity magnitude distribution

More tests are needed to prove with no doubt our assertion and this is at present a work in progress.

The novelty of the above conclusions helps to shed some light on an subject often vaguely and confusingly dealt with and implicitly affirm that full 3D computational simulations of a VAWT are feasible without having at disposal hyper-computing facilities.

From a quick glance at Figure 7, the careless reader could have been drawn to the wrong conclusion that C_P increases with grid extension in virtue of a lower downstream velocity profile. This is not at all true and the reverse exactly happens here, even in comparison with the experiments. The reason is twofold. Firstly C_P measures the shaft power and not the mechanical power left by the fluid, their link being given by the rotor efficiency. Secondly and most important, in order to correctly compute the power left by the fluid, velocity and pressure must be precisely known and taken into account at all boundaries, not only in the turbine wake. Moving the inlet BC closer raises the velocity level in the wake as well as the inlet pressure (for an assigned outlet pressure) and the laterally escaping flow rate. These two last effects prevail and, apart from efficiency considerations, C_P is higher for the "Base" grid.

After commenting the downstream velocity traverses, we turn now the attention to the profiles of turbulence intensity, displayed in Figure 8. In the experiments a phase-locked average is used to separate fluctuations from the mean value, thus filtering out every disturbance of frequency multiple than the fundamental one (20 Hertz). Vortices shed from the pole and/or the stalled blades are hence not necessarily filtered and contribute somehow to the Tu even if they are not turbulent fluctuations. Moreover, the hot-wire probe actually accurately measured only U_{rms}, that is reasonably the most important component of the velocity fluctuation in the turbine shear layers, whilst in the simulations Tu is defined assuming isotropy of the normal Reynolds stresses. Therefore the computed value should underestimate the measured one. The difference is supposed to soften in presence of strong flow separations with the associated release of turbulent vortices containing transversal velocity fluctuation of the same order of magnitude, as indeed happens at smaller TSRs.

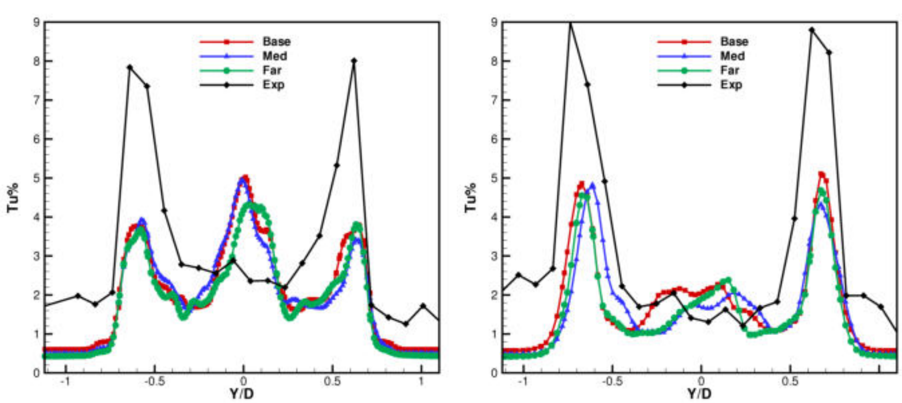

(a) $X/D = 0.75D$ (b) $X/D = 1.5D$

Figure 8: VAWT λ_1: turbulence intensity distribution

Also in this case results obtained with the three grids are quite similar one another, exhibiting two lateral peaks nicely centered with respect to the measured data. The Tu levels inside and outside the mixing layers are however underestimated and in the experiments there is no evident trace of the shaft wake. Moving downstream, the central peak associated with the wake of the rotating pole is damped; on the contrary the maximum value of turbulent kinetic energy in the two lateral mixing layer slightly increases, both in the experiment and in the simulations. The reason of the illusory contradiction lies in the different length scales of the two shear layers. The turbine wake has D as characteristic dimension whilst the shaft wake its own diameter, twenty times smaller; therefore at $X/D = 1.5$ we are in the shaft far-wake region of decaying turbulence as opposed to the near-field of the VAWT wake.

The same trends in predicted performance versus computational mesh just discussed for λ_1 can be observed in the λ_2 test cases, whose results are summarised in Table 4. The only remarkable difference is the higher root-mean-square of the pressure coefficient, now reaching values as high as 3% of $\overline{C_P}$. This is not surprising since at TSR=2.4 α varies between $\pm 24.5°$ (occurring respectively at $\theta = 115°$ and $245°$) and in the rotation lower ($90° < \theta < 270°$) and leeward ($180° < \theta < 360°$) halves each blade experiences strong separations and interactions with arriving wakes and vortices. By the way, it is not surprising that two-dimensional C_P is higher for λ_1; increasing the TSR, α_{max} is progressively reduced, eventually hindering any boundary layer separation: here λ should reach about 5.5 in order to restrict the range of the angle of attack within the steady stall limit. This trend is then reversed when the range $\pm\alpha_{max}$ is so small that the lift contribution to the torque starts to decrease and drag becomes relatively more important.

C_P values obtained in the simulations for TSR=2.4 anyway appear too low; in fact their level is smaller than the full (3D) turbine experimental datum of 0.26. The matter might be ascribed to an overestimation of fluid dynamic losses in strong stall regions, but whole causes of this behaviour will be investigated in a forthcoming work.

Notwithstanding this observation, a quite remarkable agreement with mea-

Grid	$\overline{C_P}$	$C_{P,rms} \cdot 10^2$
"Base"	0.236	0.572
"Bl"	0.219	0.640
"Far"	0.199	0.288

Table 4: VAWT λ_2: power coefficient (average and root mean square) for different cases

surements comes out from the downstream velocity and turbulence traverses (see Figures 9 and 10).

In Figure 9 both VAWT and pole wakes are well reproduced; in particular the latter widens and reduces its velocity deficit during the route from $X/D = 0.75$ to $X/D = 1.50$. Figure 10 puts to evidence three well distinct peaks of turbulence; from the highest, belonging to the lower side turbine mixing layer, to the middle one, pertaining to the shaft, and then to the smallest, referring to the upper side turbine mixing layer. It must be reminded that it is exactly in the lower part of the revolution that the blade experiences the greatest angle of attacks and moves retreating from the wind. Strong vortices start detaching from the airfoil when θ is about $100°$ and promote production of turbulent kinetic energy. Therefore at $X/D = 0.75$ the lower shear wake is already well developed and dampens its turbulence intensity going downstream. The opposite happens in the upper VAWT shear layer, akin to the evolution previously discussed in the λ_1 test case.

In order to assess the feasibility of our observations, we performed computations using both the two selected codes and thus computations on the "Base" grid were repeated using STAR-CCM+ with the same fundamental discretization ingredients (second order accurate discretization, coupled pressure-velocity approach and $k-\omega$ $low-Re$ SST model, etc). The computed $\overline{C_P}$ for the λ_1 "Base" solution is 0.417, compared with 0.385 given by Fluent; this difference is lower than 10% and, more important to say, varies consistently for the other meshes considered. We can therefore be confident that our conclusions about

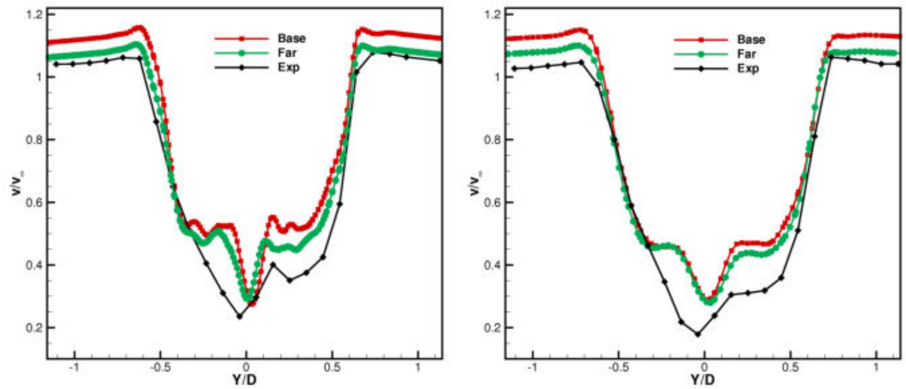

(a) $X/D = 0.75$

(b) $X/D = 1.5$

Figure 9: VAWT λ_2: velocity distribution

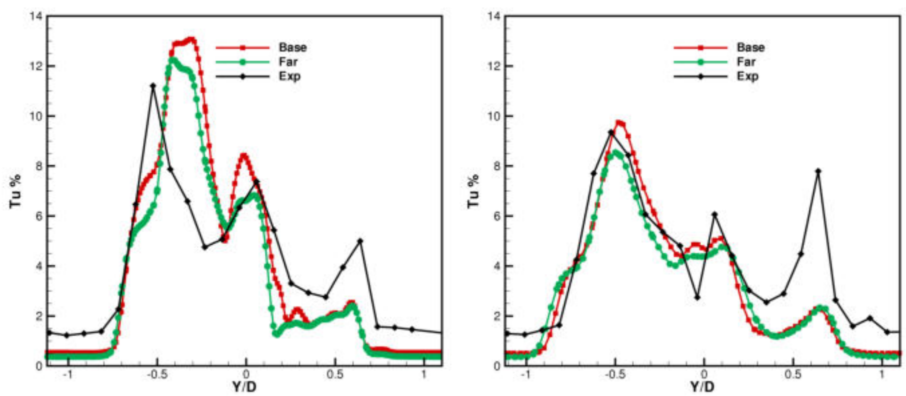

(a) $X/D = 0.75$

(b) $X/D = 1.5$

Figure 10: VAWT λ_2: turbulent intensity distribution

numerical issues are endowed with a general validity.

3.2. Critical flow analysis

Basic computations have been performed not only to investigate the space and time discretization parameters but also in order to study the behavior of a pitching isolated airfoil oscillating with a motion nearly equivalent to that occurring in the turbine. These simulations aim at evaluating the profile behavior under unsteady phenomena and neglect the interaction between the blade surfaces and wake vortical structures. In order to make a meaningful discussion, the airfoil is made to oscillate in a freestream approaching with the turbine peripheral velocity, which sets also the reference direction for the turbine drag. Even if this is of course not the direction of the relative velocity instantaneously seen by an observer moving with the blade, the procedure is fully consistent with the choice of freestream as drag reference direction when dealing with experiments on isolated pitching airfoils. If in addition the freestream speed V that runs into the pitching airfoil is made to fluctuate in time with

$$V(t) = \sqrt{U^2 + V_\infty^2 + 2UV_\infty \cos[\theta(t)]}, \tag{3}$$

all basic conditions encountered by the VAWT blade are reproduced, except the influence of both induction and preceding airfoils boundary layers and wakes. Thus we can split the turbine flow unsteadiness into three principal contributions (angle of attack, velocity magnitude, incoming shear layers) and study the relative importance of each one.

The computational grid adopted for a NACA 0021 airfoil with the associated inner rotating grid is quite similar to the one adopted for the VAWT swinging with the law of Equation (1) for $\lambda = 3.3$. As a matter of comparison, the steady variation of C_L and C_D as functions of the angle of attack, in the adequate range for the tip speed ratios considered, are shown in Figure 11 and compared with Sheldahl et al. data [26]. Of course, throughout this section C_L and C_D (per unit span) are defined by means of the chord length. Apart from the marked influence of the Reynolds number in the stalled region, it appears that the occurrence of stall is delayed in the numerical result (and thus maximum C_L is overestimated): the trends in both coefficients are however well reproduced.

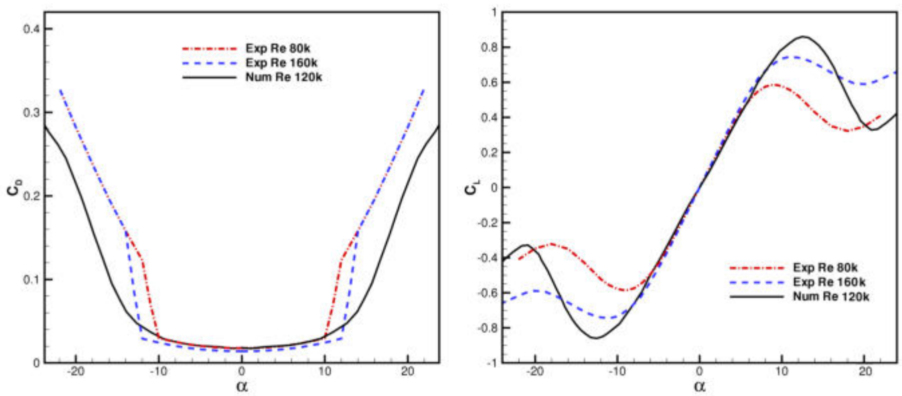

Figure 11: NACA0021: steady flow; V=U

Which is the actual impact of a Reynolds number function of the angle of attack can be appreciated by means of steady simulations under an inlet velocity V varying with α as results from Equation (3) and the functional link between θ and α for λ_1, see Figure 12.

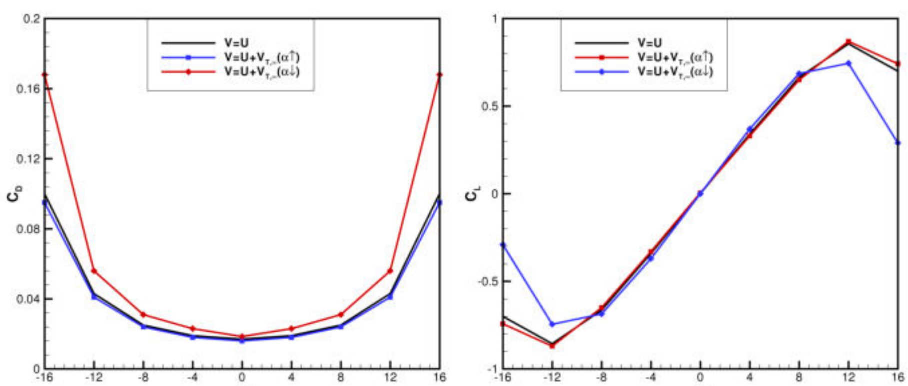

Figure 12: NACA0021: steady flow; V function of the angle of attack α

As in a turbine revolution the same α occurs twice, two graphs are presented: one in the pulling up phase ($\alpha \uparrow$) and one in the diving phase ($\alpha \downarrow$).

Figure 13 shows the lift and drag coefficients for the three cases: steady isolated, pitching isolated (constant speed), and pitching isolated (variable speed). Like before, lift and drag are made non-dimensional by means of the freestream velocity V.

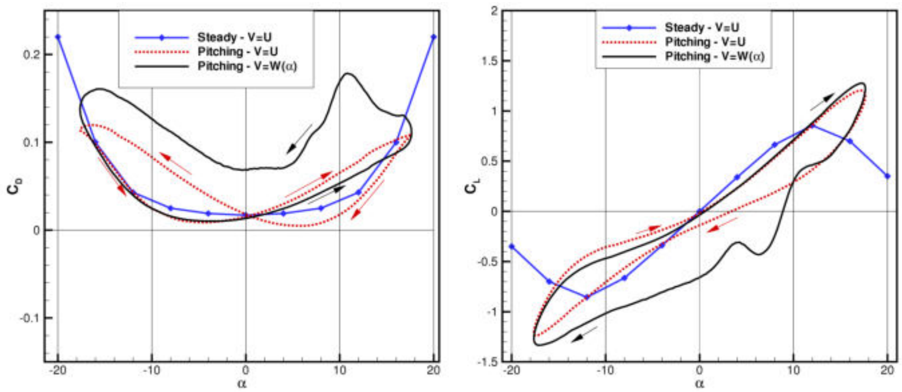

Figure 13: NACA0021: steady, pitching, and pitching-pulsating airfoil

The main differences between steady and oscillating airfoil behaviour (blue and red lines in Figure 13) in a constant wind are the broadening range of rising lift, beyond the steady stall limit, and the setting up of the hysteresis cycle. The α augmenting phase lasts much longer than the α decreasing phase (a time interval corresponding to 215 degrees of turbine rotation instead of 145) and thus the upward speed is much lower. In the C_L graph, the recovery from the stall region needs therefore a wider range of angle of attack when the airfoil is diving and, after the recovery, C_D is a little greater than in the pull-up phase. It must also be remembered that the actual angle of attack seen by an observer tied up to the airfoil should take into account the pitching motion; for instance C_L =0 in the α augmenting phase for a slightly positive angle of attack.

In addition, the lift coefficient slope in the almost linear range ($\alpha < \alpha_{stall}$) is reduced. The hysteresis is strengthened introducing the cyclical variation in freestream velocity; its minimum value is exactly midway the α decreasing phase and its maximum midway the augmenting phase. Moreover, the C_D and C_L graphs (displayed with black lines) now have lost their respectively quasi-symmetrical and quasi-antisymmetrical trait.

When comparing the variable wind pitching airfoil with the VAWT, see Figure 14, further discrepancies are evident in the whole turbine revolution. Notice that now the lift and drag coefficients of the isolated airfoil are made non dimensional by means of the peripheral velocity U and not W, for the sake of consistency with VAWT computations where use is made of a constant reference speed.

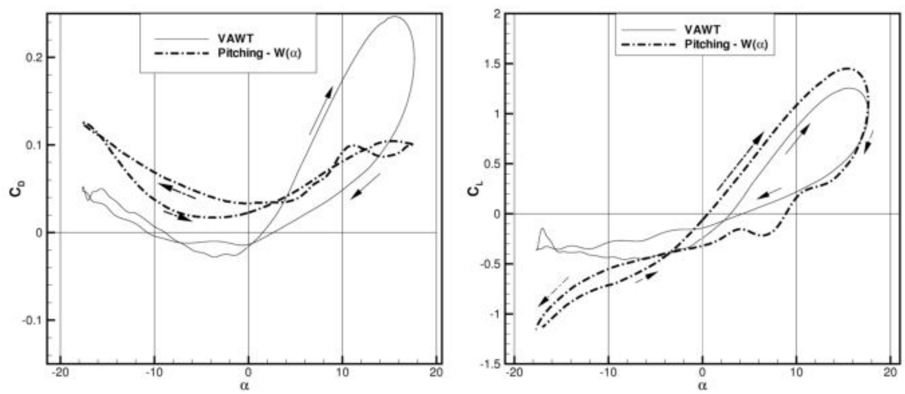

Figure 14: VAWT λ_1: C$_D$, C$_L$ of NACA0021 pitching-pulsating airfoil and VAWT

Reason of such differences is twofold: the turbine induction effect which lowers the freestream wind, as well as the magnitude of the angle of attack seen by the moving blade, and the presence of both shaft and preceding blades wakes. In the windward part of the revolution the first effect dominates, especially in the region up to α_{max} where it also causes a reduction in the magnitude of the relative velocity W. Both phenomena take part in the reduction of C_L as compared to the oscillating airfoil. At the same time, the decrease of the actual α brings on an induced drag, like the one encountered on finite wings, owing to the misalignment of the lift with respect to the undisturbed relative velocity normal direction. On the contrary, in the leeward part of the revolution, regions of low velocity fluid, due mainly to wakes and/or vortices of separated flows, yield a reduction in the magnitude of both aerodynamic coefficients.

VAWT C_L sharply falls at maximum lift, then remains nearly flat, slightly negative, in the aft-lower side and in the fourth quarter. C_D grows monotonically in the first quarter to return to normal levels in the second quarter and there remains for the rest of the revolution performing an hysteresis cycle similar to the pitching airfoil, although with smaller values.

These results show that there are big differences in the unsteady performances of oscillating airfoils as compared with a VAWT and also suggest that is not sensible to simulate the actual turbine with a simply moving single airfoil as both induction and wake effects depend heavily on the number of blades, for a given TSR.

Figure 15 displays the turbine blade drag and lift coefficients (assuming no induction to set the relative flow direction) as functions of α, while Figure 16 shows their contributions to the moment (named C_{MD} and C_{ML}) as functions of θ.

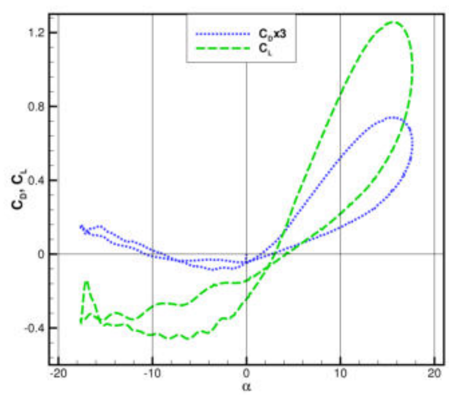

Figure 15: VAWT λ_1: drag and lift coefficients versus angle of attack

It is worth noting the difference between the angle α corresponding to the maximum lift (about 15.5°) and that of maximum torque on the axis ($\theta = 98°$, *i.e.* $\alpha = 17.4°$).

In Figure 16 C_{MD} and C_{ML} are computed supposing that, for every θ, the airfoil center of pressure is located at one fourth of the chord, *i.e.* exactly where the blade is radially connected to the shaft through the strut. Therefore, when the sum of C_{MD} and C_{ML} does not match the C_M value, the above hypothesis is not anymore valid, as distinctly happens in the downwind part of the rotation.

This is due to the simultaneous occurrence of high angle of attacks and impinging profile wakes. In addition, under these circumstances, no longer exists a blade aerodynamic center, where the torque is independent of α.

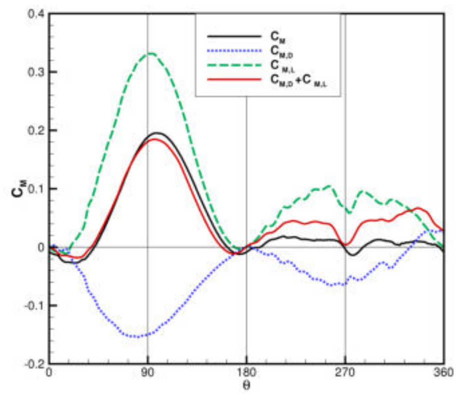

Figure 16: VAWT λ_1: moment coefficient and moment coefficients due to lift and drag, as functions of θ

3.3. VAWT flow field

We here briefly describe the flow field computed on the "Base" for the operating condition λ_1.

The aerodynamics of the turbine is characterized by inherent unsteadiness which alters significantly the blade aerodynamics among the different phases of the revolution. These features appear clearly in the present simulations, and are now discussed by resorting to the period classification proposed by Ferreira [27]. To support the flow description, instantaneous snapshots of the flow field, taken at θ equal to 0,30,60 and 90 degrees, are reported in the Figures 17–18–19. They show the contours of turbulence intensity alongside those of velocity and vorticity fields for four different azimuthal positions of the three blades; by combining different blades, and considering the 120 degree shift among each blade, these plots allow tracking the evolution of the blade aerodynamics over 12 phases over one revolution. All quantities shown are non-dimensional using the freestream wind and the chord as respectively reference speed and length, see *e.g.* the legend of Figure 19.

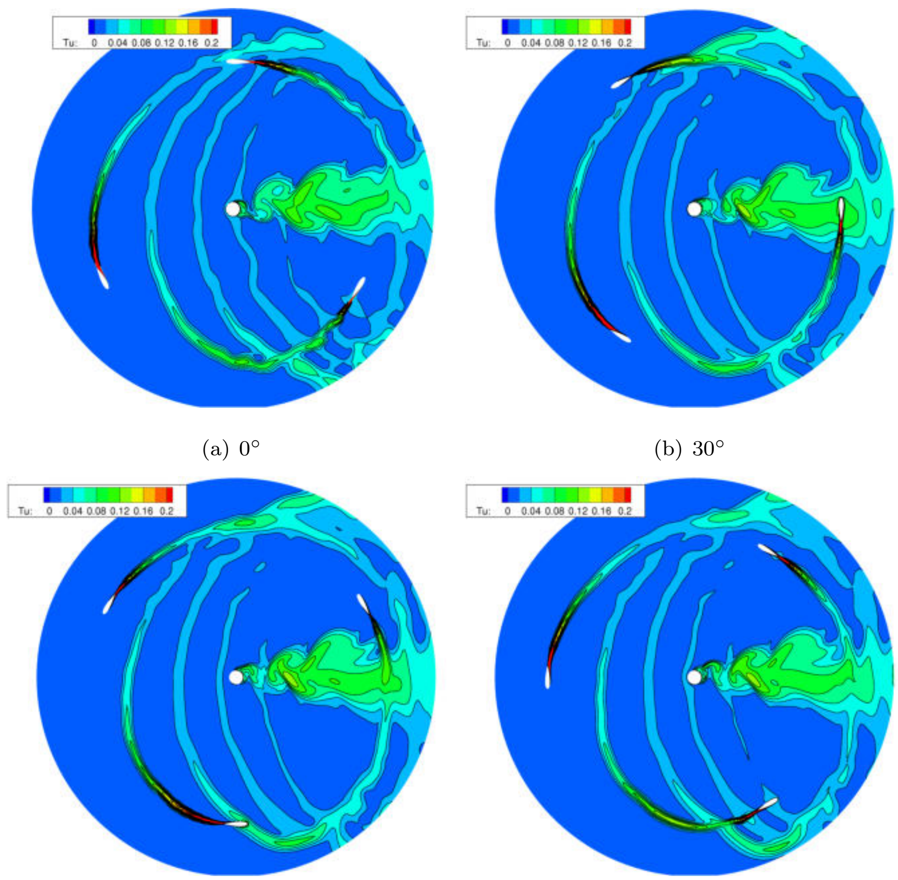

(a) 0°

(b) 30°

(c) 60°

(d) 90°

Figure 17: VAWT, λ_1: turbulence intensity contours at different angular positions θ

In the upwind quarter of revolution ($45^\circ \leq \theta \leq 135^\circ$) the blades are unperturbed by the wakes. In this period most of the power production occurs (see in Figure 16 the distribution depicted in continuous black line where the torque coefficient of the airfoil is plotted versus its angular position) and also its peak value ($\theta \approx 100^\circ$). Afterwards, in the leeward quarter of revolution ($135^\circ \leq \theta \leq 225^\circ$) the blade experiences the highest fluctuations as well as the peak values of incidence (both positive and negative, see [3]); these effects may trigger dynamic stall, with associated turbulent structures developing along the

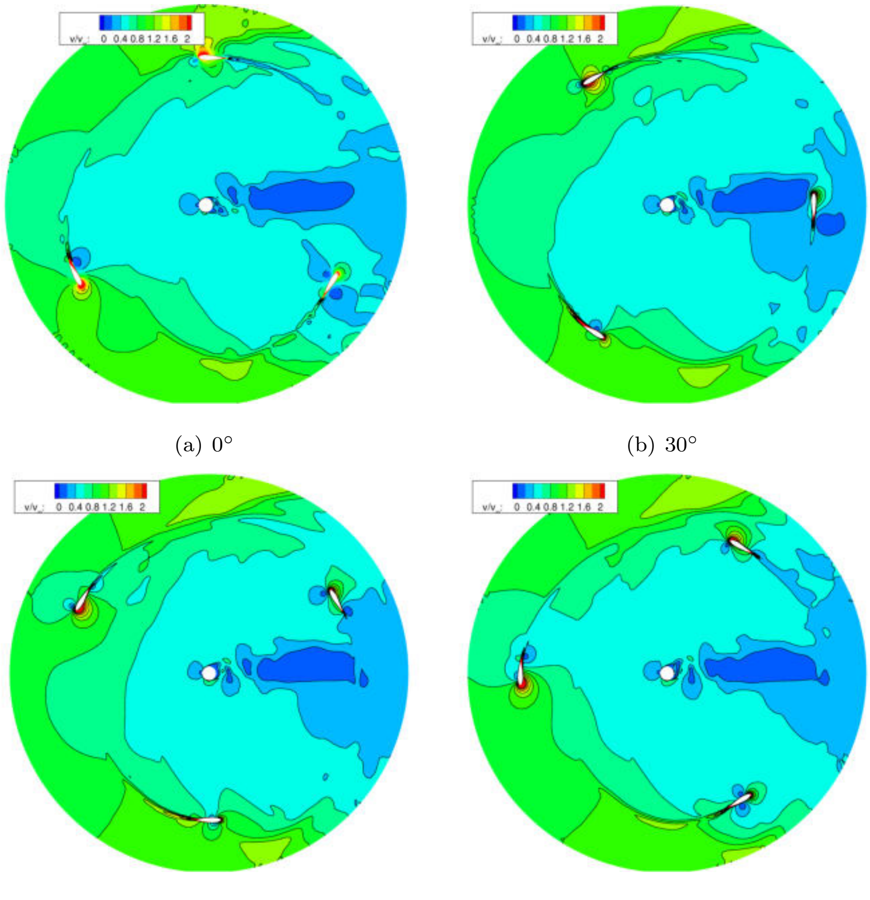

(a) 0°

(b) 30°

(c) 60°

(d) 90°

Figure 18: VAWT, λ_1: velocity magnitude contours at different angular positions θ

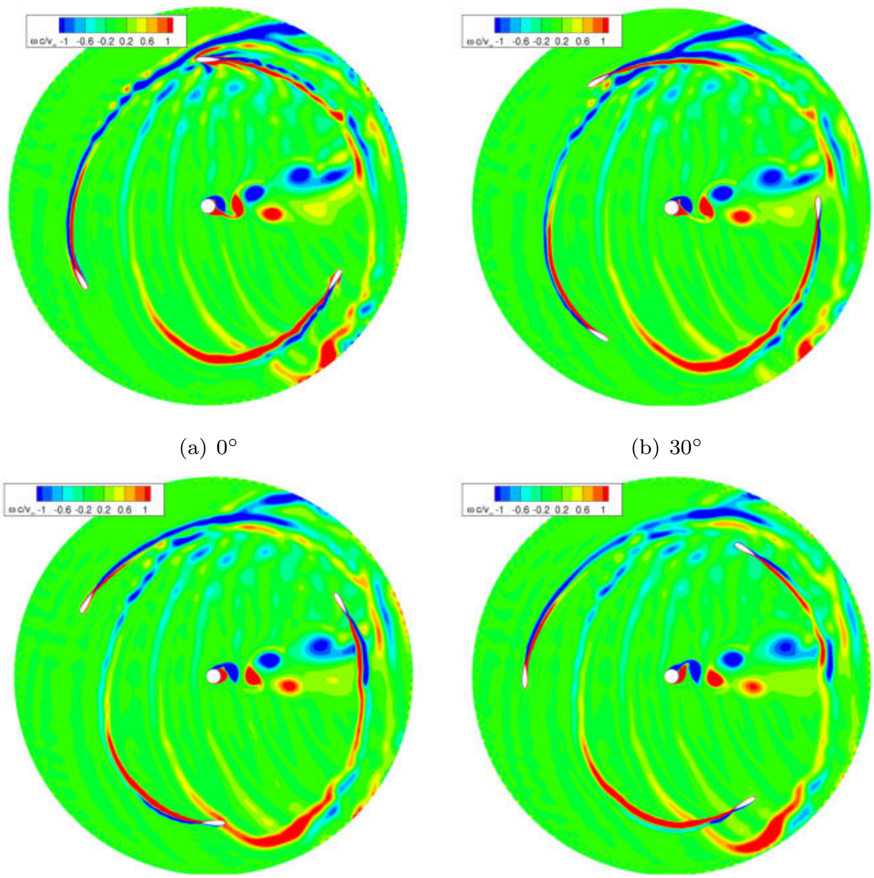

(a) 0°   (b) 30°

(c) 60°   (d) 90°

Figure 19: VAWT, λ_1: vorticity contours at different angular positions θ

blade surface from leading edge to trailing edge and viceversa (see *e.g.* [2] for a classical flow schematic on dynamic stall phenomena in VAWTs). Moreover, as clearly visible in Figure 8, in the leeward period the blade cuts the turbulent vortical structures released by both preceding blades. In the downwind period of the blade motion ($225° \leq \theta \leq 315°$) a secondary dynamic stall vortex generates an additional small peak of the lift, see *e.g.* [28], with associated slight rise of torque coefficient. In this quarter, no significant wake-blade interaction appears, even though high levels of turbulence kinetic energy and vorticity are associated to the von Karman vortex street shed by the pole. The interaction of the moving blade with the wake of the pole also leaves a trace in the trend of torque coefficient, which becomes negatiAmonge at θ of about 270 deg.

The same class of contour plots extracted for the λ_2 test case, reported in Figures 20–21–22, show the same features observed for λ_1, but with much wider and stronger flow structures: leading and trailing edge vortex formation, flow detachment, wake shedding and wall layer interaction with the turbulent structures. It is to be noted that the isocontour level values in the legends of Figures 20 and 22 are twice as those pertaining to the λ_1 case. Flow detachment on the blades starts to occur for θ equal to 90 deg and, and in the whole leeward quarter of the period counter-rotating vortices are continuously shed, so to generate a compact whirling wake across which the blade moves. In the windward quarter of the period, instead, the blade aerodynamics appears more stable and the interaction on the wakes of the other blades negligible.

4. Three-dimensional results

3D computations have been performed (with STAR-CCM+) to investigate the complex flow structures due to the blade, strut, and shaft interaction with wakes and vortices. In order to proper understand the relative importance of these phenomena, we performed a full 3D simulation and an intermediate “2.5D” calculation. The former has been run considering the symmetry of the turbine with respect to the horizontal midspan plane, as in the experimental

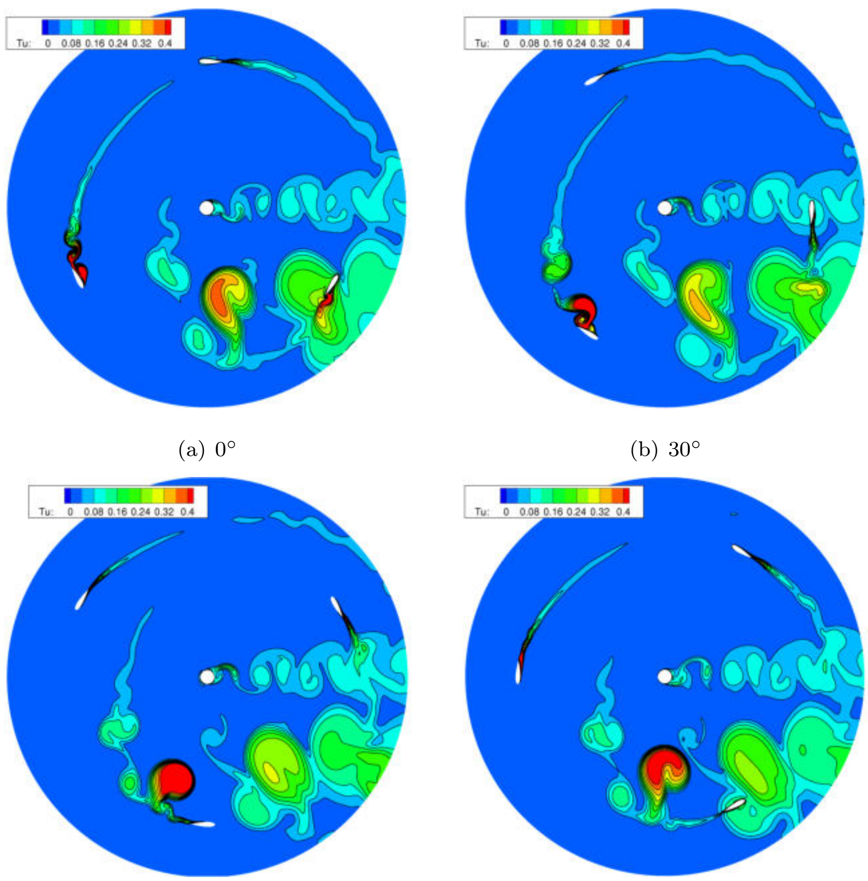

(a) 0°

(b) 30°

(c) 60°

(d) 90°

Figure 20: VAWT, λ_2: turbulence intensity contours at different angular positions θ

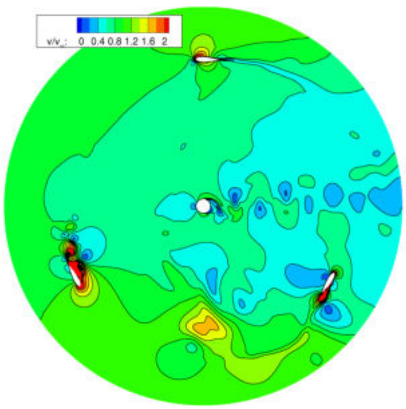

(a) 0°

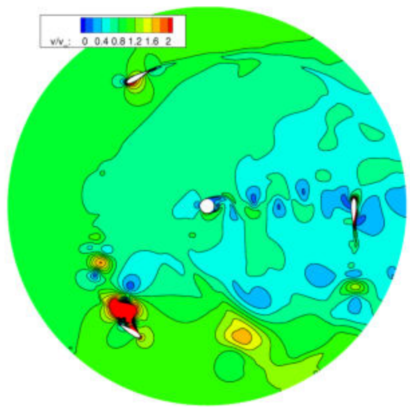

(b) 30°

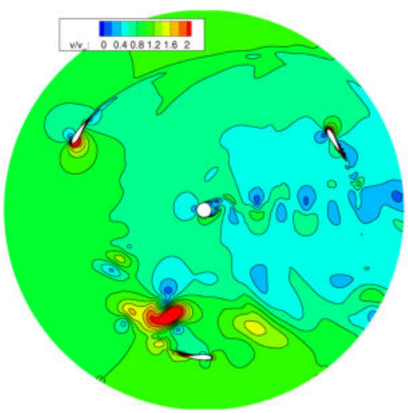

(c) 60°

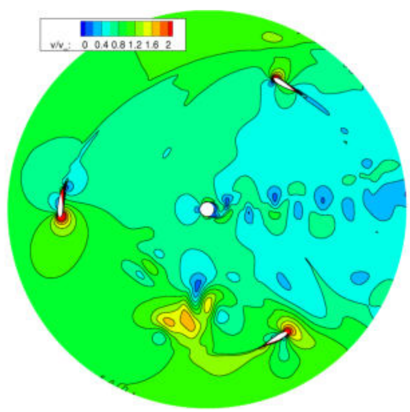

(d) 90°

Figure 21: VAWT, λ_2: velocity magnitude contours at different angular positions θ

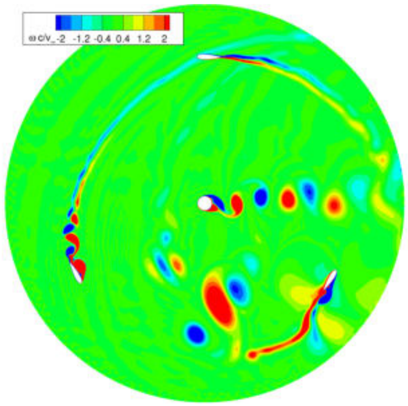

(a) 0°

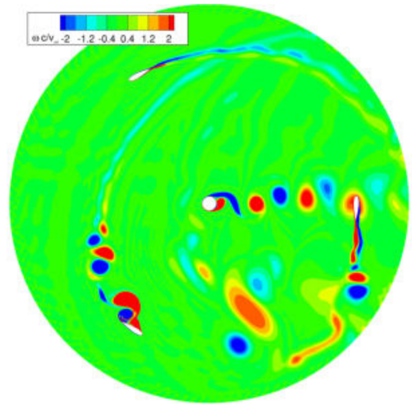

(b) 30°

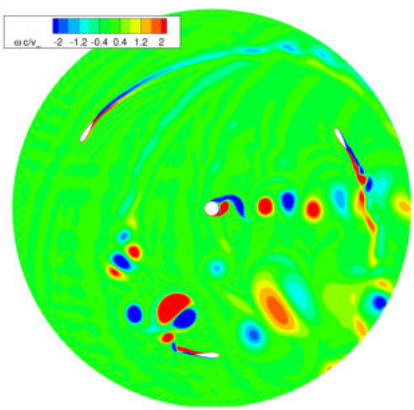

(c) 60°

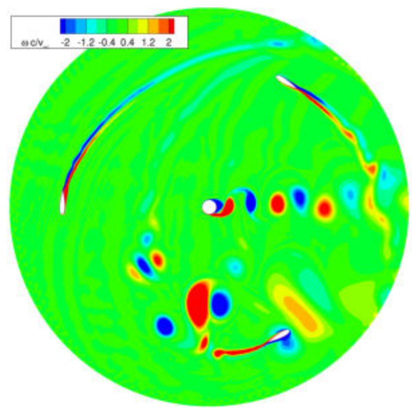

(d) 90°

Figure 22: VAWT, λ_2: vorticity contours at different angular positions θ

configuration, and thus only half machine has been modeled. The latter is named 2.5D since it considers a reduced blade height in the spanwise direction, two chords starting from the plane of the struct, which is assumed to be a local plane of symmetry. By doing so, the target is to quantify the 3D effects that can be ascribed to the presence of the strut only.

The grids have been generated following the guidelines defined in the 2D computations and similar grid spacings have been employed, although regions far enough from strong gradients were made coarser in order to save computational resources. The number of elements along the blades and within the boundary layers are indeed very similar to those adopted in the 2D case. Out of the near wall regions both grids are of polyhedric type; by virtue of this choice the total number of elements (and hence the RAM storage requirement) is greatly reduced, even if the number of faces is still sufficiently high to guarantee a good numerical resolution, as further demonstrated by the results presented in the following. Figures 23 and 24 display the two grids employed and the details of the rotating turbine zone near solid walls. The former is composed of about three millions of elements, while the latter of about eight millions.

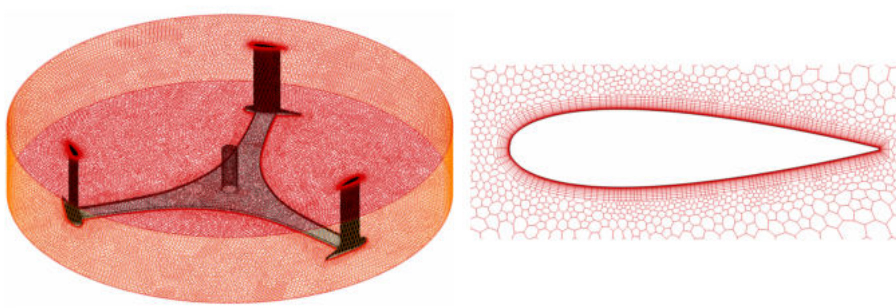

Figure 23: 2.5D grid inner (rotating) part: general view and airfoil detail

Calculations have been run for the operating conditions λ_1. Whilst 2D effects are generally more important for lower λ values, as discussed in section 3.3, 3D effects grow in quantitative relevance with the overall turbine loading, which

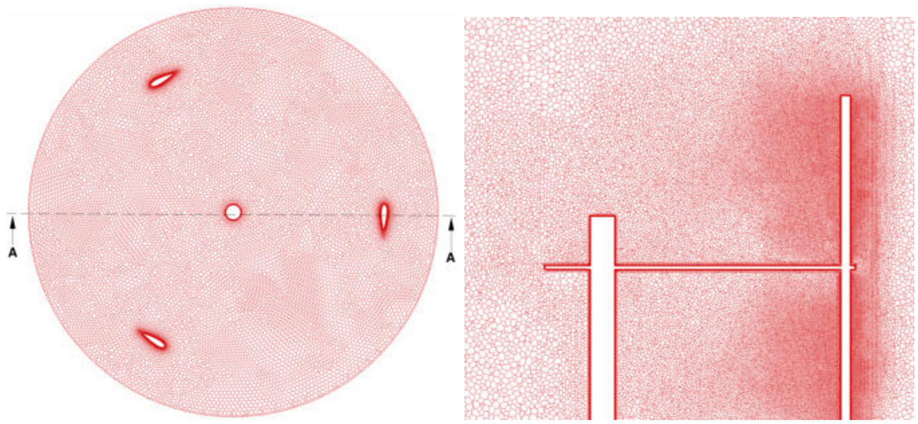

Figure 24: 3D grid inner (rotating) part: top and side views

rises with increase of relative and peripheral velocity as compared with the wind speed. Specifically, blade tip vortices depend on the loading, *i.e.* on the relative velocity, and friction on the holding structure (struts and pole) depends on the peripheral velocity. These physical considerations are confirmed, for the turbine under consideration, by the experimental findings presented in [21]. Moreover, for higher λ values wakes are more slowly convected downstream and hence each moving blade cuts many of them within one revolution period; because of the longer lasting vortical structure, higher λ operating conditions show stronger interference of the turbine parts with the flow structures.

The performance of the VAWT in presence of the strut (C_M^*) can be obtained from a linear combination of 2.5D and 2D turbine moment coefficients, namely

$$C_M^* = C_{M,2.5D}\frac{4c}{H} + C_{M,2D}\frac{H-4c}{H} \tag{4}$$

It results in about one third less driving torque as compared to the purely 2D case, reducing the C_P value to 0.28.

When the fully 3D simulation is considered, another performance reduction of the same order of magnitude occurs and $C_{P,3D} = 0.157$. Therefore, in this particular case, strut friction and blade finite length are almost equally responsible for fluid dynamic losses. The relatively large amount of these effects is partly due to the blunt (i.e., non-aerodynamic) profile of the struts, to the straight (non tapered) blade of the H-shape rotor in absence of any tip winglet, and to the TSR adopted.

The computed $C_{P,3D}$ is in excellent agreement with the experimental datum ($C_{P,exp}$=0.16). This is a very significant result, since it was achieved with a commonly affordable computational cost, and must be throughly examined on a local basis.

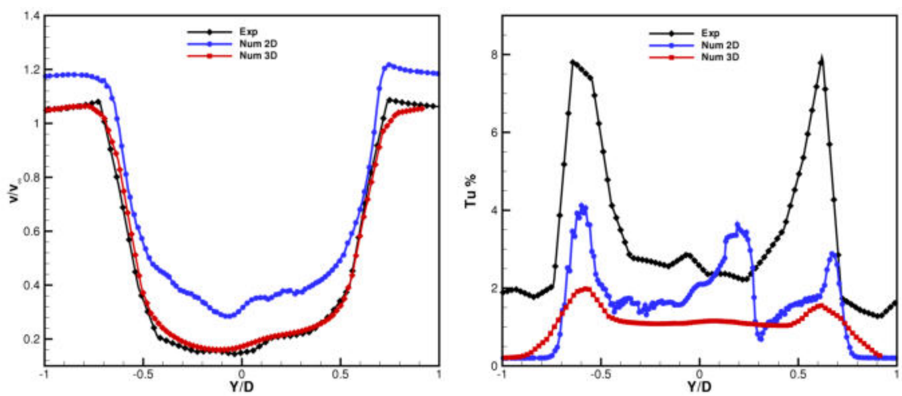

Figure 25: VAWT λ_1 3D: velocity magnitude and turbulence intensity distribution at $X/D = 0.75$ at midspan

Figure 25 shows the wake profiles on the midspan section of the turbine, in terms of velocity magnitude and turbulence intensity, obtained from measurements and both 2D and 3D simulations. As already observed, a clear overestimation of the velocity magnitude both outside and inside the turbine wake is noticeable in the 2D simulation. Much better prediction of the wake velocity profile is found when using the 3D flow model, even though the numerical set-up is exactly the same. This is an indication that, for this class of wind turbines, the application of a fully 3D flow model allows obtaining more realistic results also at midspan, and not just where severe 3D effects are generated. It should be noted that these 3D simulation was performed with the "Base" computational domain, where boundaries are placed just a few diameters far from the center of rotation. As a matter of fact, in the real 3D environment there is more room for the flow to adjust itself around the turbine, thanks to the freedom allowed by the outward spanwise motion, thus reducing the blockage effect.

Concerning the turbulence intensity profile, the 3D simulation qualitatively captures the trend highlighted by the experiments, even though peak values appear markedly underestimated, also with respect to the 2D simulation. We have already stressed the fact that, in the experiments, only the streamwise component of the unresolved velocity fluctuation is measured and that is considered "turbulence" any disturbance not multiple of the fundamental frequency (the rotational frequency times the number of blades). Another aspect is the observed difference between 2D and 3D simulations. This might be due to either the slightly lower spatial resolution of the 3D mesh or to the migration of low-inertia fluid caused by the spanwise flow component, obviously absent in a 2D flow model.

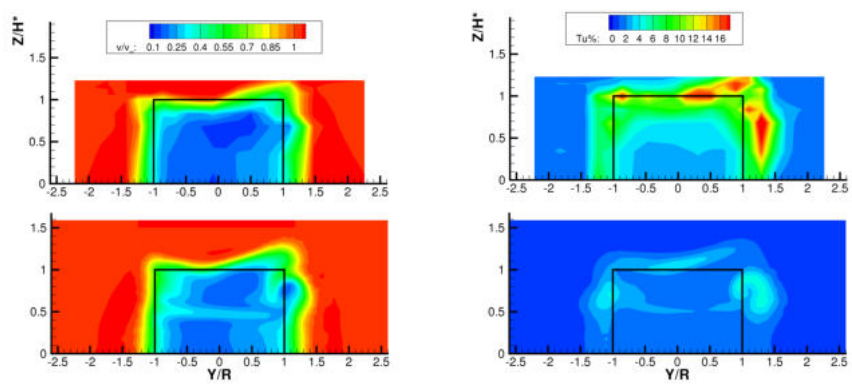

Figure 26: VAWT λ_1 3D: experimental/numerical (top/bottom) velocity and turbulence intensity contours at $X/D = 0.75$

Figure 26 shows the distribution of non dimensional velocity and turbulence intensity on the whole available measurement plane downstream of the turbine, which covers the top half of the turbine wake and extends beyond the turbine tip so to properly detect the flow structures evolving in this area.

A very good agreement is again visible in the whole velocity field. A clear trace of the strut velocity deficit can not be seen in the measurements since data were actually recorded at $Z/H^* = 0.342$ and 0.684, namely far enough from $Z/H^* = 0.5$ to do not capture the strut viscous wake; however, experiments show an effect of the struts, i.e. the wake enlargement at $Y/R = 1$ for 0.7 ¡ Z/H^* ¡ 0.8, due to the roll-up of the strut wake / boundary layer in a vortex, well captured by the simulations. A recent experimental campaign with a denser measurement grid confirmed the presence of the kink in the isolines at $Z/H^* = 0.5$.

With reference to the turbulence intensity, the qualitative distribution appear fairly well reproduced in the simulation, notwithstanding the quantitative differences, with higher values concentrated just above the blade height and/or in the "windward" side of the wake shear layer. Similarly to the experiments, it is shown a clear reduction in turbulence level approaching midspan below Z/H^* $= 0.5$.

Streamwise (X-component) vorticity contours in the same plane (see Figure 27) nicely highlight the traces of the tip vortices of alternating signs (positive upwind and negative downwind) detached from the blade end, as well as the evolution of the strut wall boundary layers. It is well apparent the lack of symmetry in the wake behind the VAWT rotor.

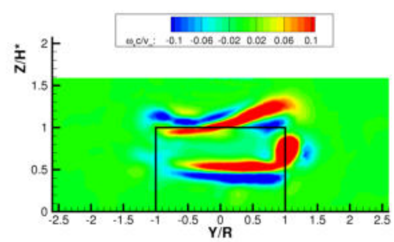

Figure 27: VAWT λ_1 3D: X-vorticity contours at $X/D = 0.75$

In order to give a more detailed picture of the VAWT complex flow field, instantaneous snapshots of fluid dynamic quantities are taken in the orthogonal planes illustrated in Figure 28.

Among the various possible locations, the azimuthal position $\theta = 30°$ was

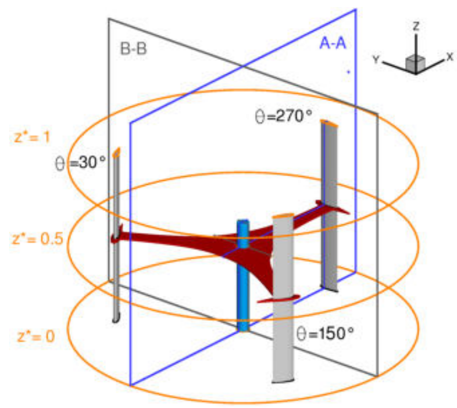

Figure 28: Reference z^* planes and normal sections

selected as, in this cut, one blade is aligned in the streamwise direction after the pole (perfectly downwind), and the other twos are symmetrically placed, respectively in the windward and leeward phases of the revolution. A-A is the longitudinal plane of the turbine and B-B is the transverse one, passing through the center of rotation. In Figure 29 the chosen variable is the vorticity component in the normal direction, thereby showing in each picture the "in-plane" vortices. Contours of the vorticity, velocity and turbulence intensity computed at different blade height z^* are displayed in Figure 30 to show the different structures charactering 2the VAWT at midspan, near the strut and at the blade tip.

First considering the distribution on the B-B plane, two clear traces of the blade trailing vorticity appear on the two sides of the traverse. The two vorticity cores exhibit a significant difference in magnitude and size; this difference is originated by the asymmetric aerodynamic loading of the blade on the advancing and retreating phases, that eventually leads to a stronger tip vortex on the right side of the image. This is, again, fully consistent with the experimental findings discussed in [21] and is the reason why a larger positive vorticity core appears on the right side of the wake in Figure 27. The stream-wise evolution of trailing vorticity core can be properly appreciated on the A-A plane. Note that whilst the X-component of the vorticity changes sign across $\theta = 90°$, the

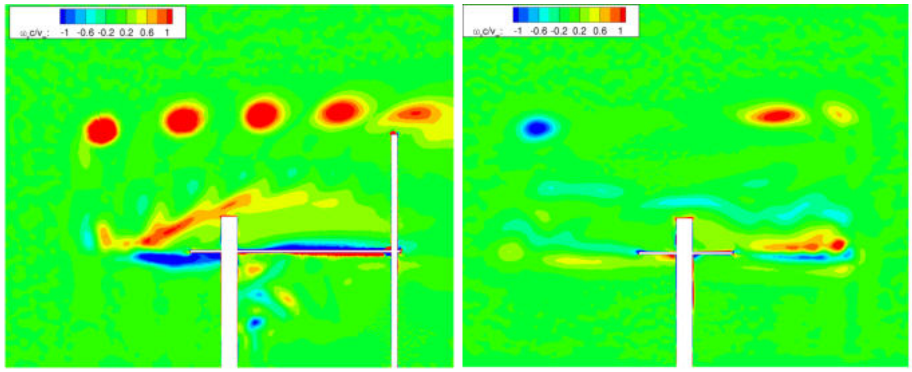

(a) A-A　　　(b) B-B

Figure 29: VAWT 3D: vorticity contours at azimuthal position $\theta = 30°$

Y-component is always positive. It is interesting to remark that the three-dimensional morphology of the vorticity field provides a confirmation of the vortex model proposed in [29].

The vorticity distribution on the A-A plane also shows the detailed vortical structures generated by the struts and the pole, and their intense interaction with the downstream blade. The viscous structures generated in the upwind part of the turbine affect blade aerodynamics for a very significant portion of the span; this provides a further indication of the high quantitative impact of the strut and of the finite blade length on the turbine performance.

Figure 31 shows, for the same azimuthal blade positions, the instantaneous streamtraces whirling across and around the turbine with a 3D perspective. Such image well illustrates the complexity of the VAWT aerodynamics and, at the same time, shows that a proper computational set-up allows capturing detailed three-dimensional flow features as well as reliable estimates of load level and performance, with a reasonable computational cost. This makes the proposed flow model relevant for both scientific and technical purposes.

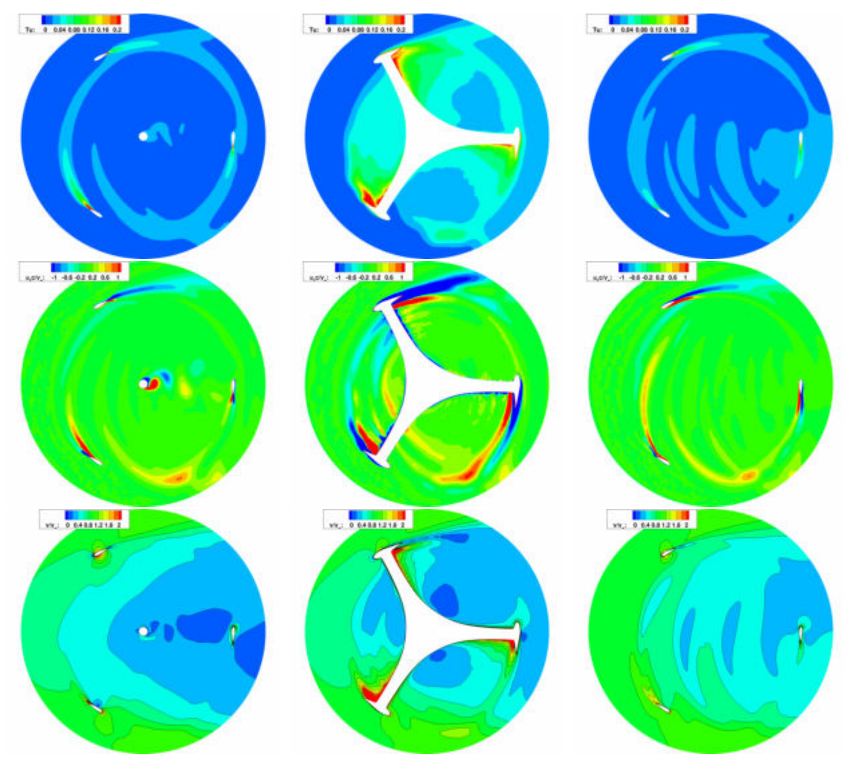

(a) $z^* = 0$ (b) $z^* = 0.5$ (c) $z^* = 1$

Figure 30: VAWT λ_1 3D: turbulence intensity, vorticity and velocity contours on the symmetry, midspan, and tip sections at $\theta = 30°$

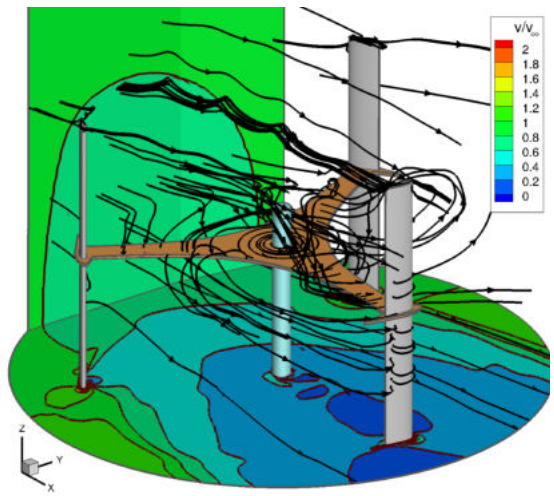

Figure 31: VAWT 3D: velocity contours and streamlines at azimuthal position $\theta = 30°$

5. Final remarks

This paper has presented a computational investigation on a small-scale Vertical Axis Wind Turbine (VAWT) for micro-generation. By virtue of a systematic comparison with real-scale wind-tunnel experiments on the investigated turbine, a dedicated assessment study has been proposed to identify the optimal parameters required for a proper modeling of the complex unsteady aerodynamics of VAWT rotors.

In particular, it has been shown that, by prescribing a specific set of boundary conditions, the dimension of the domain to be simulated can be greatly reduced with respect to common approaches found in literature; also, the inflow boundary condition has been found to be the most critical and the most influencing the quality of the solution. From this perspective, the main outcome of the assessment study is that conclusions drawn from 2D simulations are not confirmed by corresponding 3D calculations. In particular, the fully 3D nature of the flow around VAWTs has significant implications also on the flow distribution at midspan, resulting in a less restrictive condition in actual 3D modeling than that inferred from 2D simulations.

The computed flow field resulting from application of the assessed model has been investigated in detail to highlight the most relevant aerodynamic features of the rotor; to this end, a critical flow analysis has been proposed for the unsteady evolution of the aerodynamic forces on the blades, for the impact of the struts and for the rotor tip aerodynamics. The unsteady aerodynamics of the blades has been studied in comparison to steady-state data and to dedicated simulations with oscillating airfoils; results have shown that the induction effect and, especially, the interaction with the viscous wakes shed by the pole and by the blade themselves alter the aerodynamic forces, with high quantitative impact on the torque and power generated by the turbine. The presence of non-aerodynamic struts has been shown to induce a significant local loss generation, which reduced by almost one third the performance of the turbine based on 2D simulations. Finally, the complex trailing vorticity released in the wake in the tip region of the blade has been investigated, showing that (as originally observed in the available experiments) the vortices generated by the blades in the windward part of their retreating motion are the strongest ones, and also the most persistent ones in the downstream wake.

The very good agreement found between the experiments and the 3D simulation on the whole wake extension, corroborated by the excellent quantitative agreement between the measured and computed performance, indicates that 3D calculations of VAWT aerodynamics are possible also with an industrially-relevant computational cost. Future investigations will extend the present study to low tip speed ratio operating conditions, in which severe dynamic stall occurs, and to further VAWT architectures.

Acknowledgements

The authors wish to acknowledge Eng. Otman Kouaissah for his support in performing STAR-CCM+ computations.

Bibliography

[1] L. Battisti, E. Benini, A. Brighenti, S. Dell'Anna, M. R. Castelli, V. Dossena, G. Persico, U. Paulsen, T. Pedersen, Wind Tunnel Testing of the DeepWind Demonstrator in Design and Tilted Operating Conditions, Energy 111 (2016) 484–497.

[2] N. Fujisawa, S. Shibuya, Observations of dynamic stall on Darrieus wind turbine blades, Journal of Wind Engineering 89 (2001) 201–214.

[3] I. Paraschivoiu, Wind Turbine Design: With Emphasis on Darrieus Concept, Polytechnic International PressISBN 9782553009310.

[4] S. Wang, D. Ingham, L. Ma, M. Pourkashanian, Z. Tao, Numerical investigation on dynamic stall of low Reynolds number flow around oscillating airfoils, Comp. & Fluids 39 (2010) 1529–1541.

[5] K. M. Almohammadi, D. Ingham, M. Pourkashanian, Modeling dynamic stall of a straight bladed vertical axis wind turbine, J. of Fluids and Structures. 57 (2013) 144–158.

[6] L. Chao, Z. Sonye, X. You-Lin, X. Yiqing, 2.5D large eddy simulation of vertical axis wind turbine in consideration of high angle of attack, Renewable energy 51 (2013) 317–330.

[7] A. Bianchini, F. Balduzzi, G. Ferrara, L. Ferrari, G. Persico, V. Dossena, L. Battisti, Detailed analysis of the wake structure of a straight-blade H-Darrieus wind turbine by means of wind tunnel experiments and CFD simulations, Journal of Engineering for Gas Turbines and Power 140 (032604).

[8] A. Orlandi, M. Collu, S. Zanforlin, A. Shires, 3D URANS analysis of a vertical axis wind turbine in skewed flows, Journal of wind engineering and industrial aerodynamics 147 (2015) 77–84.

[9] H. Lam, H. Peng, Study of wake characteristics of a vertical axis wind turbine by two- and three-dimensional computational fluid dynamics simulations, Renewable energy 90 (2016) 386–398.

[10] A. Untariou, H. Wood, P. Allaire, R. Ribando, Investigation of self-starting capability of vertical axis wind turbines using a computational fluid dynamics approach, Journal of solar energy engineering - ASME 133 (2011) 041010–1–8.

[11] A. Rezaeiha, I. Kalkamn, B. Blocken, CFD simulation of a vertical axis wind turbine operating at a moderate tip speed ratio: guidelines for minimum domain size and azimuthal increment, Renewable energy 107 (2017) 373–385.

[12] F. Balduzzi, J. Drofelnik, A. Bianchini, G. Ferrara, L. Ferrari, M. Campobasso, Darrieus wind turbine blade unsteady aerodynamics:a three-dimensional Navire-Stokes CFD assessment, Energy 128 (2017) 550–563.

[13] F. Balduzzi, A. Bianchini, G. Ferrara, L. Ferrari, Dimensionless numbers for the assessment of mesh and timestep requirements in CFD simulations of Darrieus wind turbines, Energy 97 (2016) 246–261.

[14] F. Trivellato, M. Raciti Castelli, On the Courant-Friederics-Lewy criterion of rotating grids in 2D vertical-axis wind turbine analysis, Renewable energy 62 (2014) 53–62.

[15] F. Bassi, A. Ghidoni, A. Perbellini, S. Rebay, A. Crivellini, N. Franchina, M. Savini, A high-order discontinuous Galerkin solver for the incompressible RANS and $k-\omega$ turbulence model, Comput. & Fluids 98 (2014) 54–68.

[16] F. Balduzzi, A. Bianchini, G. Ferrara, L. Ferrari, Dimensionless numbers for the assessment of mesh and timestep requirements in CFD simulations of Darrieus wind turbines, Energy 97 (2016) 246–261.

[17] A. Rossetti, G. Pavesi, Comparison of different numerical approaches to the study of the H-Darrieus turbines start-up, Renewable energy 50 (2017) 7–19.

[18] L. Battisti, G. Persico, V. Dossena, B. Paradiso, M. Castelli, A. Brighenti, E. Benini, Experimental benchmark data for h-shaped and troposkien VAWT architectures, Renewable Energy 125 (2018) 425–444.

[19] E. Mercker, J. Wiedemann, On the correction of the inter-ference effects in open jet wind tunnels, in: SAE Technical paper, no. 960671, 1996.

[20] G. Persico, V. Dossena, B. Paradiso, L. Battisti, A. Brighenti, E. Benini, Time-resolved Experimental Characterization of Wakes Shed by H-Shaped and Troposkien Vertical Axis Wind Turbines, ASME Journal of Energy Resources Technology 139 (031203).

[21] V. Dossena, G. Persico, B. Paradiso, L. Battisti, S. Dell'Anna, E. Benini, A. Brighenti, An Experimental Study of the Aerodynamics and Performance of a Vertical Axis Wind Turbine in a Confined and Unconfined Environment, ASME Journal of Energy Resources Technology 137 (051207).

[22] F. R. Menter, Two-equation eddy-viscosity turbulence models for engineering applications, AIAA Journal 32 (8) (1994) 1598–1605.

[23] Fluent ANSYS® – Academic Research - release 17.0.

[24] StarCCM+, release xx, http://www.cd-adapco.com/products/.

[25] D. C. Wilcox, Turbulence Modelling for CFD, DCW industries Inc., La Cañada, CA 91011, USA, 2006.

[26] R. Sheldahl, P. Klimas, Aerodynamic characteristics os seven symmetrical airfoil sections through 180-degree angle of attack for use on aerodynamic analysis of vertical axis wind turbines, Sandia National Laboratories, energy report Sand80-2114, Sandia (1981).

[27] C. S. Ferreira, The near wake of the vawt, Ph.D. thesis, TU-Delfte (2009).

[28] M. Raffel, J. Kompenhans, P. Wernert, Investigation of the unsteady flow velocity field above an airfoil pitching under deep dynamic stall conditions, Experiments in fluids 19 (1995) 103–111.

[29] Battisti, L. Zanne, S. Dell'Anna, V. Dossena, G. Persico, B. Paradiso, Aerodynamic measurements on a vertical axis wind turbine in a large scale wind tunnel, Journal of Energy Resources Technology 133.